Research Square

Preprints are preliminary reports that have not undergone peer review.
They should not be considered conclusive, used to inform clinical practice,
or referenced by the media as validated information.

Fabrication of 2D Bimetallic Metal-Organic Frameworks with Enhanced Oxidase-Like Activity for AA/ALP Sensing and Antibacterial Application

Wei Li
Guilin University of Technology
Shujing Zhou
Guilin University of Technology
Jiale Hu
Guilin University of Technology
Yihong Nan
Guilin University of Technology
Pei Luo
Guilin University of Technology
Yun Zhang
Guilin University of Technology
Ziyuan Li
Guilin University of Technology
Zhongsheng Yi
Guilin University of Technology
Jianmei Zou
2019136@glut.edu.cn
Guilin University of Technology

Research Article

Keywords: 2D bimetal-organic framework, Oxidase-like activity, Colorimetric sensing, Antibacterial activity

Posted Date: February 24th, 2026

DOI: https://doi.org/10.21203/rs.3.rs-8847666/v1

License: This work is licensed under a Creative Commons Attribution 4.0 International License.
Read Full License

Additional Declarations: No competing interests reported.

Abstract

Nanozymes have garnered significant interest in sensing and antibacterial applications. In this work, a two-dimensional (2D) bimetallic cobalt/copper-based metal-organic framework (Co/Cu-MOF) was synthesized for the first time via a simple and economical one-step co-precipitation method at room temperature. The as-prepared Co/Cu-MOF showed prominent oxidase (OXD)-like activity, effectively catalyzing the decomposition of dissolved oxygen (O_2) to produce superoxide anions ($\bullet O_2^-$) and singlet oxygen ($^1O_2$). These reactive oxygen species (ROS) subsequently oxidized the colorless chromogenic substrate 3,3',5,5'-tetramethylbenzidine (TMB) into its blue oxidation product (oxTMB) without the addition of H_2O_2, yielding a characteristic absorption peak at 652 nm. The presence of ascorbic acid (AA) reduced oxTMB, resulting in a noticeable decolorization of the system. Based on this phenomenon, a novel colorimetric sensing platform was developed for quantitative detection of AA, with a linear range of 0.1–28 μM and a detection limit of 0.091 μM (3σ/m). Moreover, by employing AA as a mediator, the strategy was extended to alkaline phosphatase (ALP) detection, as ALP enzymatically hydrolyzes L-ascorbic acid-2-phosphate (AAP) to generate AA. The assay exhibited a linear response to ALP in the range of 0.2–6.5 U/L, with a detection limit of 0.12 U/L. The proposed sensor was successfully applied to the determination of AA and ALP in human serum samples. Furthermore, Co/Cu-MOF displayed strong antibacterial activity against both *Escherichia coli* (*E. coli*) and *Staphylococcus aureus* (*S. aureus*), and its underlying antibacterial mechanism was elucidated. Collectively, this 2D bimetallic MOF provides a promising platform for biochemical sensing and antimicrobial technologies.

Introduction

Natural enzymes, as highly efficient and specific biocatalysts, can catalyze biochemical reactions in living organisms and have been widely used across various fields [1]. However, their inherent drawbacks such as high production costs, poor stability, low recyclability, and sensitivity to operating conditions have greatly restricted their widespread adoption in practical applications [2]. Nanozymes, a class of nanomaterials with intrinsic enzyme-like activities, serve as ideal alternatives to natural enzymes due to their notable advantages, including high stability, low cost, tunable catalytic properties, and favorable recyclability [3–5]. Since Gao et al. first reported that Fe_3O_4 nanoparticles exhibited peroxidase (POD)-like activity [6], a wide range of nanomaterials, such as metal nanoparticles [7, 8], metal oxides [9, 10], and carbon-based nanomaterials [11], have been extensively studied and shown to exhibit predominantly POD-like or oxidase (OXD)-like activities. In contrast to POD-like nanozymes, OXD-like nanozymes can catalyze the direct conversion of O_2 into reactive oxygen species (ROS) without H_2O_2, thereby avoiding detection errors and environmental issues associated with the volatility, instability, and self-decomposition of H_2O_2 [12]. However, the practical use of OXD-like nanozymes is hampered by insufficient catalytic activity and ambiguous catalytic mechanisms. Thus, developing effective strategies to boost their catalytic performance remains a hot topic in nanozyme research.

Metal-organic frameworks (MOFs), a class of porous crystalline materials assembled from metal nodes and organic ligands, are exceptionally promising candidates for designing OXD-mimicking nanozymes because of highly tunable pore structures, abundant active sites, and large specific surface areas [13]. Consequently, numerous MOF-based biosensors have recently been developed for detecting diverse analytes, including pesticides [14], antibiotics [15], heavy metal ions [16], bacterial pathogens [17], and other targets [18, 19]. For example, Xiong et al. reported a Ce-based MOF with OXD-like activity for colorimetric detection of biothiol [20]. Similarly, Zhu et al. synthesized a vanadium-based MOF for bioenzyme-free colorimetric sensing of organophosphorus pesticides [21]. Despite their enhanced nanozyme activity, these single-metal MOFs typically require complex synthesis procedures. Moreover, their three-dimensional (3D) bulk morphology, characterized by large particle size and poor aqueous dispersibility, results in slow diffusion rates, inefficient mass transfer, and limited accessibility to active sites. These inherent limitations ultimately constrain their practical applicability in biosensing and catalytic applications.

Designing strategies to enhance the catalytic activity of MOF-based nanozymes constitutes a major challenge. From the perspective of catalyst structure, two-dimensional (2D) MOF nanosheets exhibit distinct advantages over traditional 3D bulk MOFs, including a higher specific surface area, efficient charge transport, highly accessible and exposed active sites, and rapid reactant diffusion, which have made them garner significant research interest in recent years [22]. From the perspective of catalyst composition, bimetallic MOFs, which incorporate two distinct metal ions as nodes, show superior catalytic performance to their single-metal counterparts. This enhancement arises from the second metal's ability to effectively modulate the electron density and electronic structure of the host metal [23]. Thus, the integration of a 2D architecture with two distinct metal ion nodes to construct 2D bimetallic MOFs serves as a robust strategy for enhancing the catalytic performance of MOF-based OXD-mimics.

The accurate quantification of reactive small molecules and enzymes is essential for elucidating their biological functions, assessing their physiological and pathological impacts, and enabling the diagnosis of associated diseases [24]. As a key representative, ascorbic acid (AA) serves as a critical regulator in human metabolic pathways. Its deficiency is known to cause scurvy, whereas excessive intake can induce adverse effects such as diarrhea, urinary stones, and gastric discomfort [25]. Alkaline phosphatase (ALP), an important exocrine enzyme, plays a fundamental role in regulating diverse biological processes. Abnormal ALP activity is strongly associated with multiple disorders, including bone diseases, cardiovascular conditions, cancers, and inflammation-related ailments [26]. Consequently, the development of simple, rapid, and efficient detection methods for AA and ALP is of considerable importance for early clinical diagnosis and effective disease management. Over the past decades, a range of analytical techniques have been established for AA and ALP detection, including colorimetric assays, fluorescence spectroscopy, magnetic relaxation switching (MRS), electrochemical sensors, and surface-enhanced Raman scattering (SERS) [27–31]. Among these, colorimetric methods have garnered substantial interest due to their notable advantages such as low cost, operational simplicity, fast response, good reproducibility, and minimal instrumental requirements. Notably, MOF-

based colorimetric platforms have recently emerged as promising tools for the sensitive and selective determination of AA and ALP, which has attracted growing research attention [32].

In this study, a 2D bimetallic Co/Cu-MOF was synthesized for the first time via a facile and economical one-step co-precipitation method at room temperature (Scheme 1). The obtained Co/Cu-MOF was systematically characterized to investigate its morphology, microstructure, composition, and catalytic mechanism. Results revealed that the 2D Co/Cu-MOF exhibits remarkably enhanced OXD-like activity, enabling the direct oxidation of 3,3',5,5'-tetramethylbenzidine (TMB) to produce a blue color in the absence of H_2O_2. Specifically, the bimetallic MOF exhibited over 64.1-fold higher OXD-like activity than corresponding monometallic Co-MOF. Utilizing this property, a straightforward colorimetric sensing platform was constructed for the detection of AA and ALP, which was then employed for measuring both analytes in human serum. Furthermore, leveraging the outstanding OXD-like activity of the Co/Cu-MOF, its antibacterial performance was evaluated, demonstrating significant inhibitory effects against *Escherichia coli* (*E. coli*) and *Staphylococcus aureus* (*S. aureus*). Owing to its low cost, facile synthesis, high OXD-like catalytic activity, and good reproducibility, the Co/Cu-MOF demonstrates considerable promise for biosensing and antimicrobial applications.

2. Experiments

2.1. Materials and equipment

Cobalt nitrate hexahydrate ($Co(NO_3)_2·6H_2O$), copper nitrate trihydrate ($Cu(NO_3)_2·3H_2O$), zinc nitrate hexahydrate ($Zn(NO_3)_2·6H_2O$), AA, 2-methylimidazole (2-MIM), potassium chloride (KCl), L-histidine (L-His), L-arginine (L-Arg), L-cystine (L-Cys), L-tryptophan (L-Trp), and L-tyrosine (L-Tyr), p-Benzoquinone (p-BQ) were obtained from Aladdin Biochemical Technology Co., Ltd. (Shanghai, China). L-Alanine (L-Ala), L-ascorbic acid-2-phosphate (AAP) and ALP were supplied by Shanghai Maclean Biochemical Co., Ltd. L-Lysine (L-Lys) was purchased from Shanghai Wokai Pharmaceutical Co., Ltd. (Shanghai, China). L-Serine (L-Ser) was purchased from Beijing Bailingwei Technology Co., Ltd. (Beijing, China). Fructose (Fru), D-galactose (D-Gal), lactose (Lac), 3,3',5,5'-tetramethylbenzidine (TMB), and L-proline (L-Pro) were sourced from Shanghai Yien Chemical Technology Co., Ltd. (Shanghai, China). Sucrose (Suc), glucose (Glu), sodium chloride (NaCl), acetic acid (CH_3COOH), anhydrous sodium acetate (CH_3COONa), anhydrous magnesium chloride ($MgCl_2$), and aluminum nitrate nonahydrate ($Al(NO_3)_3·9H_2O$) were provided by Xilong Chemical Co., Ltd. Anhydrous ethanol ($CH3CH_2OH$) was acquired from Tianjin Fuyu Fine Chemical Co., Ltd. Maltose (Mal) was obtained from Lizhu Dongfeng Biotechnology Co., Ltd. Luria-Bertani (LB) broth and agar powder were purchased from Beijing Soleibao Technology Co., Ltd. Gram-negative *E. coli* (ATCC 8739) and Gram-positive *S. aureus* (ATCC 6538) were procured from the Guangdong Microbial Culture Collection Center. All chemicals were of analytical grade and used as received unless otherwise specified. Human serum samples were obtained from a university hospital. Deionized water (specific resistivity ≥ 18.2 MΩ·cm⁻¹), generated by an ultrapure water

system (UPS-II-20L, Chengdu Yuechun Technology Co., Ltd.), was employed to prepare all stock solutions.

Ultraviolet-visible (UV-Vis) absorption spectra of the samples were recorded on a LAMBDA 365 UV-Vis spectrophotometer (PerkinElmer, Shanghai, China). The crystal phase of the as-synthesized product was characterized via X-ray diffraction (XRD, PANalytical, Netherlands). X-ray photoelectron spectroscopy (XPS) characterization was carried out on a Kratos AXIS HSI spectrometer. The morphology of the Co/Cu-MOF and bacteria was analyzed using scanning electron microscopy (SEM; Hitachi SU5000, Japan) and transmission electron microscopy (TEM; JEM-2100F, JEOL, Japan), respectively. Additionally, the optical density at 570 nm (OD_{570}) values of the bacteria were recorded on an iMark™ microplate reader (Bio-Rad Laboratories, USA).

2.2. Fabrication of 2D bimetallic Co/Cu-MOF

The 2D bimetallic Co/Cu-MOF was synthesized through a facile, one-step co-precipitation route adapted from a literature method with minor modifications [33]. In a typical synthesis, 0.6624 g of $Co(NO_3)_2 \cdot 6H_2O$ and 0.3666 g of $Cu(NO_3)_2 \cdot 3H_2O$ (corresponding to a Co:Cu molar ratio of 6:4) were dissolved in 105 mL of deionized water to form the metal precursor solution. Separately, 1.8 g of 2-methylimidazole was dissolved in another 105 mL of deionized water. Under continuous stirring, 20 mL of the mixed metal solution was added to 20 mL of the 2-methylimidazole solution. The mixture was stirred at room temperature for 2 h and then allowed to stand in the dark at room temperature for 24 h. Afterward, the supernatant was discarded, and the precipitate was washed twice with deionized water and three times with anhydrous ethanol, followed by centrifugation at 5000 rpm for 5 min after each washing step. The resulting solid was dried at 60°C for 4 h. Finally, the obtained Co/Cu-MOF was stored in a desiccator for subsequent use.

2.3 Assessing the OXD-like catalytic activity and steady-state kinetics of 2D bimetallic Co/Cu-MOF

The OXD-like catalytic activity of the 2D bimetallic Co/Cu-MOF was investigated via the TMB oxidation assay. Briefly, 50 μL of a Co/Cu-MOF dispersion (300 μg/mL) and 50 μL of TMB solution (4 mM) were added into 400 μL of acetate buffer (0.1 M, pH 4.0). After reacting at room temperature for 10 min, the UV-Vis spectrum was recorded with a UV-vis spectrophotometer.

Steady-state kinetic assays for the OXD-like activity of Co/Cu-MOF were performed using TMB as the substrate at varying concentrations (0.18–0.7 mM). The initial reaction velocities were determined by monitoring the increase in absorbance at 652 nm over time. The apparent kinetic parameters (K_m and V_{max}) were derived by fitting the data to the Michaelis-Menten equation:

$$\frac{1}{V_0} = \frac{K_m}{V_{max}} \frac{1}{[S]} + \frac{1}{V_{max}}$$

where V_{max} and K_m represent the maximum reaction velocity and the Michaelis constant, respectively, V_o is the initial velocity, and [S] denotes the substrate concentration.

2.3. Colorimetric detection of AA and ALP

Briefly, a 450 μL catalytic reaction system was prepared by mixing 30 μL of Co/Cu-MOF dispersion (500 μg/mL), 40 μL of TMB solution (5 mM), and 380 μL of NaAc-HAc buffer (0.1 M, pH 4.0). This mixture was initially incubated at room temperature for 10 min. After the introduction of 50 μL AA solutions with gradient concentrations, the reaction mixture was subjected to thorough vortexing and further incubated for 5 min. Finally, the absorbance value of the result solution at 652 nm was determined using a UV-Vis spectrophotometer.

For the colorimetric detection of ALP, 50 μL of L-ascorbic acid-2-phosphate (AAP; 1 mM) and 50 μL of ALP solutions at varying concentrations were added to 100 μL of Tris-HCl buffer (0.01 M, pH 8.0). The mixture was then incubated at 37°C for 40 min. Subsequently, 50 μL of this reaction solution was added to 450 μL of the catalytic reaction system (as described above), and the reaction was allowed to proceed at room temperature for 10 min. Finally, the absorbance of the final solution at 652 nm was measured using a UV-Vis spectrophotometer.

To investigate the potential interference of other compounds on the detection of AA and ALP, selectivity tests were conducted using the most common interfering species. The tests were performed following the same procedure, wherein the target analytes (20 μM AA and 6 U/L ALP) were individually substituted with each interferent at a concentration of 200 μM. The interferents tested included L-Pro, L-Trp, L-His, L-Cys, L-Tyr, L-Ser, L-Ala, L-Lys, L-Arg, Suc, D-Gal, Lac, Fru, Glu, KCl, NaCl, $MgCl_2$, $Zn(NO_3)_2{\cdot}6H_2O$ and $Al(NO_3)_3{\cdot}9H_2O$.

2.4. Determination of AA and ALP in human serum

To evaluate the practical applicability of the as-constructed colorimetric sensor, the concentrations of AA and ALP were determined in human serum samples. Whole blood from healthy donors was collected from the University Hospital of Guilin University of Technology, filtered through a 0.45 μm membrane to remove particulates. All pretreated samples were subsequently diluted with buffer solution to ensure that the target analyte concentrations fell within the linear detection range of the sensor. The resulting solution was spiked with graded concentrations of AA or ALP and utilized as a practical working stock solution for colorimetric assays, in accordance with the experimental protocol detailed in the preceding section.

2.5. Antimicrobial tests

The antibacterial performance of Co/Cu-MOF was evaluated using the zone of inhibition method. First, equal amounts of Co-MOF, Cu-MOF, and Co/Cu-MOF were each mixed thoroughly with an equal amount of agar powder. Then, the individual mixtures were compressed into thin circular pellets using a tablet press. The *E. coli* and *S. aureus* colonies were cultured in LB broth at 37°C. A 100 μL of the bacterial

suspension (~ 1×10^6 CFU/mL) was evenly spread onto agar plates. Subsequently, the pre-prepared material pellets were placed on the surface of the inoculated plates. After incubation at 37°C for 24 h, the diameters of the inhibition zones were measured.

The minimum inhibitory concentration (MIC) of Co-MOF, Cu-MOF, and Co/Cu-MOF was quantified via the standard liquid dilution method. Briefly, the as-synthesized MOF powders were individually dispersed in 1 mL of pH 7.0 acetate buffer to formulate a stock suspension with an initial concentration of 3.2 mg/mL. Subsequently, these stock suspensions were diluted to a series of working suspensions with concentrations ranging from 0 to 3.2 mg/mL (0, 0.1, 0.2, 0.4, 0.8, 1.6, 3.2 mg/mL). For the MIC determination assay, 200 µL of LB broth, 500 µL of the gradient-diluted MOF suspension and 50 µL of bacterial suspension (~ 10^8 CFU/mL) were mixed thoroughly in a 96-well microplate. To assess the time-dependent inhibitory efficacy of the MOFs on bacterial proliferation, the OD_{570} of each well was monitored at predetermined time points (0, 3, 6, 9, 12, 15, 24 h) using a microplate reader.

Bacterial cultures were prepared following the aforementioned inhibition assay procedure, and the morphological alterations of bacterial cells were characterized using SEM. The bacterial suspensions were centrifuged at 6,000 rpm for 5 min at room temperature, and the supernatant was discarded. The collected bacterial pellets were immobilized in 2.5% glutaraldehyde solution at 4°C for 4 h. Subsequent to fixation, the samples underwent a gradient ethanol dehydration process with sequential immersion in 30%, 50%, 70%, 90%, and 100% (v/v) ethanol solutions, with each treatment step lasting 15 min. After air-drying, the samples were freeze-dried for 24 h to obtain a powdered specimen. Finally, the microstructural features of the bacteria were characterized via SEM.

3. Results and discussion

3.1. Synthesis and characterization of 2D bimetallic Co/Cu-MOF

A novel two-dimensional bimetallic MOF was synthesized through a simple one-step co-precipitation approach at room temperature, employing cobalt (Co) and copper (Cu) as dual catalytic centers with 2-methylimidazole as the organic ligand. The corresponding monometallic Co-MOF and Cu-MOF were also prepared under the same experimental conditions for comparative studies. The materials were characterized using several techniques. SEM characterization revealed that Co-MOF exhibited a smooth, spindle-shaped rod-like morphology with micrometer-scale dimensions (Fig. 1A), whereas Cu-MOF featured a thin plate-like nanostructure with well-defined edges (Fig. 1B). Upon bimetallic incorporation, the as-fabricated Co/Cu-MOF partially inherited the morphology characteristic of the Cu-MOF (Fig. 1C). TEM further confirmed a two-dimensional hexagonal nanosheet structure for Co/Cu-MOF, with its lateral dimensions ranging from 400 to 700 nm (inset in Fig. 1C). Elemental mapping analysis verified the homogeneous spatial distribution of Co, Cu, O, N and C throughout the Co/Cu-MOF matrix, which evidenced the successful incorporation of both metal ions into a single MOF (Fig. 1D).

The crystal structures of Cu-MOF, Co-MOF, and bimetallic Co/Cu-MOF were characterized via XRD. As shown in Fig. 1E, the diffraction peak positions of Co/Cu-MOF were nearly consistent with those of its monometallic counterparts (Cu-MOF and Co-MOF), demonstrating that the simultaneous incorporation of Co^{2+} and Cu^{2+} preserved a comparable crystalline framework. In contrast, the overall diffraction peak intensity of Co/Cu-MOF was markedly diminished relative to the monometallic MOFs, implying a lower crystallinity and a potential reduction in crystallite size [34]. Notably, the diffraction signals associated with the (011) and (112) crystal planes were significantly attenuated in Co/Cu-MOF, which revealed that the coexistence of Co and Cu impaired the periodic atomic arrangement or structural integrity along these crystallographic orientations. Furthermore, a slight positive shift of several diffraction peaks was detected, arising from lattice strain or local structural distortion induced by the coexistence of the two metal species.

XPS measurements were carried out to investigate the elemental composition and surface oxidation states of the Co/Cu-MOF. As expected, the XPS full spectrum further confirmed the coexistence of Co, Cu, O, N and C in the Co/Cu-MOF (Fig. 1F). In the high-resolution Co 2p spectrum (Fig. 1G), well-resolved peaks were observed at 781.16 eV and 797.05 eV, which were assigned to Co^{3+} $2p_{3/2}$ and Co^{3+} $2p_{1/2}$, respectively; additional characteristic signals at 784.72 eV and 803.00 eV corresponded to Co^{2+} $2p_{3/2}$ and Co^{2+} $2p_{1/2}$. The high-resolution Cu 2p XPS spectrum (Fig. 1H) showed two prominent main peaks at 933.69 eV ($2p_{3/2}$) and 954.68 eV ($2p_{1/2}$), accompanied by two distinct shake-up satellite peaks at 941.88 eV and 963.01 eV, which are characteristic of the Cu^{2+} oxidation state. Additionally, a peak observed at 930.04 eV is assigned to the Cu^{+} $2p_{3/2}$ state. Collectively, the above results confirm the successful fabrication of the 2D bimetallic Co/Cu-MOF.

3.2. Enhanced OXD-like activity and catalytic mechanism of 2D bimetallic Co/Cu-MOF

Following the successful synthesis of the 2D bimetallic Co/Cu-MOF, its OXD-like activity was systematically investigated. TMB, a widely utilized chromogenic substrate for OXD activity assays that can be oxidized to its intensely colored product (oxTMB) with a characteristic absorbance peak at 652 nm [35], was chosen as the substrate. As shown in Fig. 2A, the pristine TMB solution was colorless and exhibited no obvious UV-vis absorption within the range of 500–800 nm. Upon the addition of Co/Cu-MOF, the solution turned dark blue and displayed a distinct absorption peak at 652 nm, confirming the formation of oxTMB. However, when the TMB solution was first deaerated with N_2 to remove dissolved O_2, the absorption at 652 nm decreased substantially. These results demonstrated that O_2 was an essential prerequisite for the catalytic reaction. The Co/Cu-MOF facilitated the activation of dissolved O_2 to ROS, which in turn were responsible for the oxidation of TMB. Thus, in accordance with previous reports [36], the as-fabricated Co/Cu-MOF exhibited OXD-like activity.

Previous literature indicates that OXD-like catalysts typically generate $^1O_2$, •OH and $•O_2^-$ radicals during substrate oxidation [36]. To identify the dominant ROS involved in the catalytic process, ROS-scavenging

experiments were conducted using mannitol (for •OH), p-BQ (for $•O_2^-$) and Trp (for $^1O_2$) as selective scavengers. The analysis of the radical inhibition efficiency revealed that the TMB oxidation activity in the Co/Cu-MOF system decreased by 0%, 83.3% and 75% with mannitol, p-BQ and Trp, respectively, indicating that $•O_2^-$ and $^1O_2$ are the dominant reactive species for the catalytic oxidation of TMB (Fig. 2B).

Furthermore, the catalytic performance of the 2D bimetallic Co/Cu-MOF was compared with that of its monometallic counterparts under identical experimental conditions. As displayed in Fig. 2C, upon the addition of Co-MOF, the solution turned pale blue and the absorbance at 652 nm was still very low, indicating the weak OXD-like activity of Co-MOF. Meanwhile, Cu-MOF induced neither color change nor detectable absorption, confirming its lack of OXD-like catalytic activity. By contrast, the introduction of Co/Cu-MOF resulted in a deep blue solution and a robust absorbance peak at 652 nm, revealing that the OXD-like catalytic activity of Co/Cu-MOF was markedly enhanced. This remarkable activity enhancement may be attributed to the synergy between the dual metal centers and the 2D morphological feature of Co/Cu-MOF, which forms a cooperative catalytic system. In this system, the two metal species exert a synergistic effect via electronic and structural modulation, thus efficiently accelerating electron transfer and significantly improving the efficiency of the TMB catalytic oxidation reaction. To further enhance the catalytic performance of Co/Cu-MOF, the mass ratio of Co^{2+}:Cu^{2+} and synthesis time were systematically optimized. The results indicated that the Co/Cu-MOF achieved optimal catalytic activity at a Co^{2+}:Cu^{2+} mass ratio of 3:2 with a synthesis time of 2 h (Fig. S1).

In order to further study the kinetics and catalytic activity of Co/Cu-MOF as an oxidase mimic, steady-state kinetic measurements were carried out with varying TMB concentrations. As shown in Fig. 2D, the system's absorbance at 652 nm exhibited a significant enhancement with increasing reaction time and TMB concentration. Corresponding Michaelis-Menten kinetics confirmed that the reaction rate increased progressively with rising TMB concentration (Fig. 2E). Analysis of the Lineweaver-Burk plot (inset in Fig. 2E) yielded a maximum reaction rate (V_{max}) of 2.591×10^{-7} M s^{-1} for Co/Cu-MOF, representing a 64.1-fold enhancement in oxidase-like activity compared to that of Co-MOF (4.039×10^{-9} M s^{-1}, Fig. S2). Moreover, the Michaelis constant (K_m) for Co/Cu-MOF was determined to be 0.122 mM, notably lower than the 0.328 mM observed for Co-MOF. The combination of a higher V_{max} and a lower K_m indicated superior OXD-like activity and a stronger substrate affinity for the bimetallic system. This enhancement was attributed to the synergistic effects of the 2D porous framework and bimetallic doping in Co/Cu-MOF. The 2D architecture offers a large accessible surface area, promoting efficient reactant diffusion, while simultaneously exposing a high density of catalytically active sites for substrate interaction. Furthermore, bimetallic doping not only introduces lattice defects that generate additional active sites but also substantially improves electron transfer efficiency during catalysis. Density functional theory (DFT) calculations were performed using Gaussian 16 with the B3LYP method and the 6–31 + G (d, p) basis set to investigate the energy levels and optimized geometries of frontier molecular orbitals [37] [38]. These calculations examined how metal doping modulates the MOF band gap, linking such modulation to changes in enzymatic activity. From the DFT results, high-quality molecular orbital

isosurface maps were generated efficiently using Multiwfn [39] and VMD. These maps provided key mechanistic insight by showing that bimetallic doping narrows the HOMO–LUMO gap in Co/Cu-MOF compared to its monometallic counterparts (Co-MOF and Cu-MOF), thereby promoting electron transfer during the activation process (Fig. 2F). Collectively, these structural and electronic modifications account for the markedly enhanced OXD-like activity. The comparison of K_m and V_{max} of Co/Cu-MOF and other reported OXD-like materials was summarized in Table S1, which further corroborated the superior catalytic performance of Co/Cu-MOF.

3.3. Applications of 2D bimetallic Co/Cu-MOF

3.3.1. Colorimetric detection of AA and ALP

In this work, a simple sensing platform based on 2D bimetallic Co/Cu-MOF with enhanced OXD-like activity was developed for the efficient and sensitive detection of AA and ALP. The detection mechanism was illustrated in Scheme 1. The synthesized Co/Cu-MOF displayed excellent OXD-like activity and can directly catalyze the oxidation of TMB to yield a blue oxidized product (oxTMB) in the absence of H_2O_2. As an endogenous vitamin with inherent antioxidant properties, AA can scavenge ROS and reduce oxTMB to TMB via a one-electron transfer mechanism, leading to a remarkable fading of the blue color [40]. Leveraging this principle, a simple colorimetric sensor was constructed by exploiting the OXD-like activity of the Co/Cu-MOF for quantitative determination of AA. Notably, ALP catalyzes the dephosphorylation of AAP to release AA and then reduces oxTMB to TMB. Thus, using AAP as a substrate bridge, a sensitive colorimetric assay for ALP was also successfully established. As presented in Fig. 3A, the introduction of AA into the Co/Cu-MOF-TMB system caused obvious fading of the blue color, accompanied by a sharp decrease in absorbance at 652 nm in the UV-vis spectrum. This decolorization originated from the reducing capability of AA, which effectively quenches the oxidized TMB (oxTMB). By a similar mechanism, when ALP was introduced into the system containing AAP, ALP catalyzed the enzymatic hydrolysis of AAP, which generated AA in situ. The subsequent reduction of oxTMB by this enzymatically generated AA led to decolorization of the solution and a decrease in absorbance. These distinct “turn-off” colorimetric responses confirmed the feasibility of constructing a facile colorimetric assay based on the OXD-like activity of Co/Cu-MOF for the sensitive and rapid detection of both AA and ALP.

Prior to quantitative detection, key experimental parameters including reaction time, temperature, pH, and concentrations of Co/Cu-MOF and TMB were systematically investigated and optimized (Fig. S3). Under the optimized conditions, the Co/Cu-MOF-TMB system was incubated with a series of AA solutions at different concentrations, and the absorbance of the resulting mixtures was measured. As shown in Fig. 3B, increasing AA concentrations resulted in a gradual fading of the blue color, accompanied by a progressive decrease in absorbance at 652 nm. Figure 3C exhibited a robust linear correlation between the ΔA_{652} values and AA concentrations over the range of 0.1–28 μM, with the linear regression equation $y = 0.0262x + 0.0822$ and a correlation coefficient (R^2) of 0.997. The limit of detection (LOD) was calculated to be 0.091 μM according to the 3σ/S criterion. For ALP detection, the

absorbance of the reaction mixture at 652 nm also decreased with increasing ALP activity in the range of 0.2–6.5 U/L (Fig. 3D). The corresponding calibration plot for ALP activity was displayed in Fig. 3E, with the linear regression equation $y = 0.0727x + 0.03053$ ($R^2 = 0.995$), and the LOD was determined to be 0.12 U/L. In comparison with recently reported detection strategies for AA and ALP (summarized in Tables S2 and S3), the proposed sensing platform achieved a lower LOD for both analytes, which was ascribed to the exceptional catalytic efficiency of the 2D bimetallic Co/Cu-MOF.

To assess the selectivity of the proposed sensing platform for AA and ALP detection, a series of potential interferents, including L-Pro, L-Trp, L-His, L-Cys, L-Tyr, L-Ser, L-Ala, L-Lys, L-Arg, sucrose (Suc), D-galactose (D-Gal), lactose (Lac), fructose (Fru), glucose (Glu), KCl, NaCl, $MgCl_2$, $Zn(NO_3)_2{\cdot}6H_2O$, and $Al(NO_3)_3{\cdot}9H_2O$, were subjected to the identical detection conditions (Fig. 3F). A significant decrease in absorbance at 652 nm was observed only in the presence of the target analytes (20 μM AA and 6 U/L ALP). In contrast, all interferents produced negligible absorbance changes at the same wavelength. These results confirmed the excellent selectivity of the sensing platform for AA and ALP.

To further validate the practical applicability of this method for detecting AA and ALP in real samples, the concentrations and recoveries of both analytes were determined in human serum using the standard addition method under optimized experimental conditions. As summarized in Tables S4 and S5, the recovery rates of AA and ALP in human serum ranged from 91.92% to 99.47% and from 106.0% to 108.5%, respectively. The corresponding relative standard deviations (RSDs) fell within 0.43%-3.35% and 0.22%-1.89%, respectively. These results confirmed the high precision and reliability of the proposed colorimetric assay for detecting AA and ALP in complex biological matrices. Together, these findings highlight the strong practical potential of this colorimetric method for real-sample analysis.

3.3.2. The antibacterial activity and mechanism of 2D bimetallic Co/Cu-MOF

Building upon its enhanced OXD-like activity, the antibacterial performance of the 2D bimetallic Co/Cu-MOF was systematically assessed against representative Gram-negative (*E. coli*) and Gram-positive (*S. aureus*) bacteria. As displayed in Fig. 4A and 4B, Co/Cu-MOF possessed markedly stronger antibacterial effects compared to monometallic Co-MOF and Cu-MOF, as reflected by larger and clearer inhibition zones. This improvement was attributable to the combined advantages of its 2D nanostructure and bimetallic synergy. Quantitative analysis revealed that the diameters of the inhibition zones (DIZ) for Co/Cu-MOF against *E. coli* and *S. aureus* were 23 mm and 21 mm, respectively, suggesting that the Gram-negative strain is more susceptible to the MOF. This variation in sensitivity originated from fundamental differences in cell wall architecture: the thicker peptidoglycan layer characteristic of Gram-positive bacteria (*S. aureus*) can hinder the penetration of antibacterial materials, leading to enhanced bacterial tolerance relative to Gram-negative bacteria (*E. coli*) [41]. To further validate these findings, bacterial growth curve assays were conducted to corroborate the antibacterial activity. As shown in Fig. 4C-H, the minimum inhibitory concentration (MIC) of the bimetallic Co/Cu-MOF for both *E. coli* and *S. aureus* was markedly lower than those of the monometallic counterparts (Co-MOF and Cu-MOF). At

the MIC concentration, complete growth inhibition ($OD_{570} \approx 0$) was achieved within 3 h, confirming the rapid bactericidal effect of Co/Cu-MOF. Furthermore, the MIC against *E. coli* (133.3 μg/mL) was substantially lower than that against *S. aureus* (266.7 μg/mL), further demonstrating a greater potency of the Co/Cu-MOF against the Gram-negative bacterium.

Subsequent SEM analysis was conducted to evaluate morphological changes in bacteria following Co/Cu-MOF treatment. As shown in Fig. 4I and 4J, untreated *E. coli* and *S. aureus* exhibited smooth, intact morphological features. In contrast, after exposure to the Co/Cu-MOF, *E. coli* displayed significant shrinkage, alongside disruption of the cell wall and membrane (Fig. 4K). Likewise, *S. aureus* showed pronounced wrinkling and localized surface rupture (Fig. 4L). These structural alterations indicated that the Co/Cu-MOF induced substantial degradation of bacterial cellular structural integrity, which constituted a key mechanism underlying its potent, rapid antibacterial activity.

To further verify the membrane-damaging effect of the Co/Cu-MOF, protein leakage assays were performed on *E. coli* and *S. aureus* under Co/Cu-MOF stress. As shown in Fig. S4, after 24 h of incubation with the Co/Cu-MOF, the extent of protein leakage from both *E. coli* and *S. aureus* was significantly higher than that from bacteria treated with the monometallic Co-MOF and Cu-MOF, further demonstrating that the 2D nanostructure and bimetallic synergy collectively contribute to the Co/Cu-MOF's enhanced capacity to disrupt bacterial cell membranes. Furthermore, following treatment with the three types of MOFs, the extent of protein leakage from *E. coli* was greater than that from *S. aureus*, which can be attributed to the thicker peptidoglycan layer characteristic of Gram-positive bacteria. This finding indicated that bacterial membrane permeability was increased and the cell membranes were disrupted upon exposure to the Co/Cu-MOF, which is consistent with the morphological observations from bacterial SEM analysis.

Subsequently, agarose gel electrophoresis was performed to evaluate the effect of the Co/Cu-MOF on bacterial DNA integrity. Following treatment of *E. coli* and *S. aureus* with the Co/Cu-MOF at concentrations of 0, 1, 2, and 4 × the MIC, DNA band patterns were analyzed. As shown in Fig. S5, while control samples exhibited bright and distinct DNA bands, bacteria exposed to the Co/Cu-MOF showed progressively fainter or absent DNA bands. Furthermore, this disruption of genomic integrity occurred in a concentration-dependent manner. These findings indicated that the Co/Cu-MOF not only targeted bacterial cell membranes but also damaged genomic DNA, thereby likely compromising the DNA's biological functions.

4. Conclusion

In summary, we have successfully synthesized a 2D bimetallic Co/Cu-MOF nanozyme with enhanced OXD-like activity. The straightforward synthesis of the Co/Cu-MOF, combined with its superior catalytic performance as indicated by the lower K_m values derived from steady-state kinetic analysis, underscored its efficiency. The enhanced activity was primarily attributed to the synergistic effect between the dual metal centers and the unique 2D porous architecture of the material, which facilitated efficient

decomposition of O_2 into substantial amounts of reactive oxygen species ($\bullet O_2^-$ and $^1O_2$). These ROS exhibited strong oxidative capacity toward TMB. Based on this excellent catalytic behavior, we constructed a simple and efficient colorimetric sensing platform for the detection of AA and ALP, achieving detection limits of 0.091 μM and 0.12 U/L, respectively. Furthermore, Co/Cu-MOF demonstrated potent antibacterial activity. Its antibacterial mechanism was proposed to follow a sequential process: initial disruption of bacterial membrane integrity, subsequent DNA damage, and ultimately cell death. Overall, the as-prepared 2D bimetallic Co/Cu-MOF represents a highly promising material for applications in biosensing and biomedical applications.

Declarations

Consent to participate

Informed consent was obtained from all individual participants included in the study

Ethical approval statement

Human whole blood samples used in this study were collected from healthy individuals and provided by the affiliated hospital of Guilin University of Technology (Guilin, China) with informed consent and under the approval ethics committee of the affiliated hospital of Guilin University of Technology. The studies have been performed in accordance with the ethical standards.

Funding Declaration

This work was financially supported by the National Natural Science Foundation of China (No. 22264011), Natural Science Foundation of Guangxi Province (No. 2020GXNSFBA297114), and Scientific Research Staring Foundation of Guilin University of Technology (No. GUTQDJJ2019136).

Conflicts of interest

There are no conflicts to declare.

Author contributions

Wei Li: Conceptualization, Methodology design, Formal analysis, Data curation, Resource coordination, Writing-Original draft, Writing-Review & editing. Shujing Zhou: Methodology, Actual sample collection and analysis, Data curation, Formal analysis. Jiale Hu: Data collection, Formal analysis, Investigation. Yihong Nan: Data collection, Investigation, Validation. Pei Luo: Formal analysis, Visualization. Yun Zhang: Writing-Review & editing, Investigation. Ziyuan Li: Data collection, Formal analysis, Validation. Zhongsheng Yi: Project administration. Jianmei Zou: Writing-Review & editing, Visualization, Investigation, Project supervision, Funding acquisition, Oversight, Project administration.

Data availability

The data supporting the findings of this study will be made available upon request.

References

1. Sheng JY, Wu YH, Ding H, Feng KZ, Shen Y, Zhang Y, Gu N (2024) Multienzyme-like nanozymes: regulation, rational design, and application. Adv Mater 36:2211210. https://doi.org/10.1002/adma.202211210.
2. Chen Z, Yu YX, Gao YH, Zhu ZL (2023) Rational design strategies for nanozymes. ACS nano 17:13062-13080. https://doi.org/10.1021/acsnano.3c04378.
3. Shen XM, Wang ZZ, Gao XJ, Gao XF (2024) Reaction mechanisms and kinetics of nanozymes: insights from theory and computation. Adv Mater 36:2211151. https://doi.org/10.1002/adma.202211151.
4. Cui X, Zhang JC, Liu YT, Shao W, Tang YW, Sun HJ (2023) A portable nanozyme-strip fabricated by Ru-ZIF-8 with dual nanozymatic activity for detection of acetylcholine. ChemNanoMat 9:e202300310. https://doi.org/10.1002/cnma.202300310.
5. Lin S, Sun SY, Wang K, Tang HM, Ran FY, Li X, Liu J (2024) Environmental responsive peroxidase-like activity of MoS_2@ halloysite nanotubes mediated by piezoelectric effect. Surf Interfaces 51:104755. https://doi.org/10.1016/j.surfin.2024.104755.
6. Gao LZ, Zhuang J, Nie L, Zhang JB, Zhang Y, Gu N, Wang TH, Feng J, Yang DL, Perrett S, Yan XY (2007) Intrinsic peroxidase-like activity of ferromagnetic nanoparticles. Nat Nanotechnol 2:577-583. https://doi.org/10.1038/nnano.2007.260.
7. Lu C, Tang LH, Gao F, Li YZ, Liu JW, Zheng JK (2021) DNA-encoded bimetallic Au-Pt dumbbell nanozyme for high-performance detection and eradication of Escherichia coli O157: H7. Biosens Bioelectron 187:113327. https://doi.org/10.1016/j.bios.2021.113327.
8. Sang XQ, Xia SY, Cheng L, Wu FX, Tian Y, Guo CX, Xu GB, Yuan YL, Niu WX (2024) Deciphering the mechanisms of photo-enhanced catalytic activities in plasmonic Pd-Au heteromeric nanozymes for colorimetric analysis. Small 20:2305369. https://doi.org/10.1002/smll.202305369.
9. Xia F, Shi QF, Nan ZD (2020) Facile synthesis of Cu-$CuFe_2O_4$ nanozymes for sensitive assay of H_2O_2 and GSH. Dalton Trans 49:12780-12792. https://doi.org/10.1039/D0DT02395G.
10. Zhang HY, Chen YT, Wei YH, Zhang XK, Ma HC (2025) Construction of a CuO_2@PDA nanozyme with switchable dual enzyme-mimic activities for colorimetric sensing of catechol and hydroquinone. ACS Appl Mater Interfaces 17:15886-15895. https://doi.org/10.1021/acsami.5c00904.
11. Muhammad P, Hanif S, Li JY, Guller A, Rehman FU, Ismail M, Zhang DY, Yan XY, Fan KL, Shi BY (2022) Carbon dots supported single Fe atom nanozyme for drug-resistant glioblastoma therapy by

activating autophagy-lysosome pathway. Nano Today 45:101530. https://doi.org/10.1016/j.nantod.2022.101530.

12. Li C, Le Q, Nan ZD (2025) Dual-enzyme-mimic activity of FeCo-MOF for colorimetric detection of cysteine and Cu^{2+}. Colloids Surf, A 708:136036. https://doi.org/10.1016/j.colsurfa.2024.136036.
13. Liu JX, Yu XY, Zhou YD, Sun LB, Liu YL, Li JY (2025) Breaking the conventional: Ligand-triggered Zn-MOF nanozyme with unusual oxidase activity for dual-channel sensing of benfuracarb. Biosens Bioelectron 280:117441. https://doi.org/10.1016/j.bios.2025.117441.
14. Gao XT, Liu MY, Lei MY, Kong YX, Xu XJ, Zhang QF (2024) A Zn-MOF-based mixed matrix membrane as an ultrastable luminescent sensor for selective and visual detection of antibiotics and pesticides in food samples. Talanta 277:126303. https://doi.org/10.1016/j.talanta.2024.126303.
15. Amani V, Norouzi F, Akrami Z (2024) A review of UiO-based MOF detection and removal strategies for antibiotics in water. New J Chem 48:18600-18617. https://doi.org/10.1039/D4NJ03409K.
16. Zhao J, Wang YN, Dong WW, Wu YP, Li DS, Zhang QC (2016) A robust luminescent Tb(III)-MOF with Lewis basic pyridyl sites for the highly sensitive detection of metal ions and small molecules. Inorg Chem 55:3265-3271. https://doi.org/10.1021/acs.inorgchem.5b02294.
17. Fatah SA, Omer KM (2025) Aptamer-modified MOFs (Aptamer@MOF) for efficient detection of bacterial pathogens: A review. ACS Appl Mater Interfaces 17:11578-11594. https://doi.org/10.1021/acsami.4c21944.
18. Zhou N, Su FF, Guo CP, He LH, Jia ZK, Wang MH, Jia QJ, Zhang ZH, Lu SY (2019) Two-dimensional oriented growth of Zn-MOF-on-Zr-MOF architecture: A highly sensitive and selective platform for detecting cancer markers. Biosens Bioelectron 123:51-58. https://doi.org/10.1016/j.bios.2018.09.079.
19. Ren JW, Ledwaba M, Musyoka NM, Langmi HW, Mathe M, Liao SJ, Pang W (2017) Structural defects in metal-organic frameworks (MOFs): Formation, detection and control towards practices of interests. Coord Chem Rev 349:169-197. https://doi.org/10.1016/j.ccr.2017.08.017.
20. Dang JQ, Zhen M, Gu JN, Niu YT, Zheng YF (2025) Ce-Based MOF nanozyme with oxidase-like activity for sensitive colorimetric detection of glutathione in periodontitis. Colloids Surf, A 727:138333. https://doi.org/10.1016/j.colsurfa.2025.138333.
21. Du NJ, Weng WC, Xu YY, Zhou Y, Yi YH, Zhao Y, Zhu GB (2024) Vanadium-based metal-organic frameworks with peroxidase-like activity as a colorimetric sensing platform for direct detection of organophosphorus pesticides. Inorg Chem 63:16442-16450. https://doi.org/10.1021/acs.inorgchem.4c02716.
22. Wang YX, Zhao MT, Ping JF, Chen B, Cao XH, Huang Y, Tan CL, Ma QL, Wu SX, Yu YF (2016) Bioinspired design of ultrathin 2D bimetallic metal-organic-framework nanosheets used as biomimetic enzymes. Adv Mater 28:4149-4155. https://doi.org/10.1002/adma.201600108.
23. Ma Q, Xue YH, Zhang CN, Chen YY, Teng W, Zhang H, Fan JW (2025) 2D copper-iron bimetallic metal-organic frameworks for reduction of nitrate with boosted efficiency and ammonia selectivity. J Environ Sci 149:374-385. https://doi.org/10.1016/j.jes.2024.01.046.

24. Chen PP, Yan SX, Sawyer E, Ying BW, Wei XW, Wu ZZ, Geng J (2019) Rapid and simple detection of ascorbic acid and alkaline phosphatase via controlled generation of silver nanoparticles and selective recognition. Analyst 144:1147-1152. https://doi.org/10.1039/C8AN01925H.
25. Wu TT, Ma ZY, Li PP, Liu ML, Liu XY, Li HT, Zhang YY, Yao SZ (2019) Colorimetric detection of ascorbic acid and alkaline phosphatase activity based on the novel oxidase mimetic of Fe-Co bimetallic alloy encapsulated porous carbon nanocages. Talanta 202:354-361. https://doi.org/10.1016/j.talanta.2019.05.034.
26. Zhang X, Ren CH, Hu F, Gao Y, Wang ZY, Li HQ, Liu JF, Liu B, Yang CH (2020) Detection of bacterial alkaline phosphatase activity by enzymatic in situ self-assembly of the AIEgen-peptide conjugate. Anal Chem 92:5185-5190. https://doi.org/10.1021/acs.analchem.9b05704.
27. Rong MC, Lin LP, Song XH, Wang YR, Zhong YX, Yan JW, Feng YF, Zeng XY, Chen X (2015) Fluorescence sensing of chromium (VI) and ascorbic acid using graphitic carbon nitride nanosheets as a fluorescent "switch". Biosens Bioelectron 68:210-217. https://doi.org/10.1016/j.bios.2014.12.024.
28. Li Y, Cai YT, Wang YY, Xue RS, Ren ZW, Liu YM, Chen W, Liu Z, Bao XF, Huang ZZ (2025) A reusable copper-cysteamine fluorescence probe for cost-effective detection of alkaline phosphatase activity based on a redox-modulated inner filter effect. Microchem J 209:112694. https://doi.org/10.1016/j.microc.2025.112694.
29. Wang H, Pu GQ, Devaramani S, Wang YF, Yang ZF, Li LF, Ma XF, Lu XQ (2018) Bimodal electrochemiluminescence of G-CNQDs in the presence of double coreactants for ascorbic acid detection. Anal Chem 90:4871-4877. https://doi.org/10.1021/acs.analchem.8b00517.
30. Dong ML, Zheng WS, Chen YP, Ran B, Qian ZY, Jiang XY (2018) Cu-T1 sensor for versatile analysis. Anal Chem 90:2833-2838. https://doi.org/10.1021/acs.analchem.7b04971.
31. Wan J, Zou JM, Zhou SJ, Pan FL, Hua F, Zhang YL, Nie JF, Zhang Y (2023) A bimetallic (Ni/Co) metal-organic framework with excellent oxidase-like activity for colorimetric sensing of ascorbic acid. Anal Methods 15:1819-1825. https://doi.org/10.1039/D2AY01927B.
32. Muhammad P, Tu XY, Liu J, Wang YJ, Liu Z (2017) Molecularly imprinted plasmonic substrates for specific and ultrasensitive immunoassay of trace glycoproteins in biological samples. ACS Appl Mater Interfaces 9:12082-12091. https://doi.org/10.1021/acsami.7b00628.
33. Zhang D, Luo N, Xue ZG, Bai YL, Xu JQ (2022) Effect of open metal sites in cobalt-based bimetallic metal-organic framework nanoparticles-coated quartz crystal microbalance (QCM) for humidity detection. ACS Appl Nano Mater 5:2147-2155. https://doi.org/10.1021/acsanm.1c03861.
34. Zhang JY, Xu GB, Zhang Q, Li X, Yang Y, Yang LW, Huang JY, Zhou GM (2022) Mo-O-C between MoS_2 and graphene toward accelerated polysulfide catalytic conversion for advanced lithium-sulfur batteries. Adv Sci 9:2201579. https://doi.org/10.1002/advs.202201579.
35. Wang XL, Li QZ, Zhao YL, Gao XF (2025) Recent advances in oxidase-like nanozymes: mechanisms, prediction models, and applications. ACS Appl Mater Interfaces 17:66110-66150. https://doi.org/10.1021/acsami.5c15196.

36. Li HR, Chen DQ, Zhou W, Cheng DH, Ge DH, Chen XJ (2023) Synergistically enhanced oxidase-like property of core-shell MOF nanozymes by decorating Au and Ag/AgCl nanoparticles for L-cysteine colorimetric sensing. Langmuir 39:16833-16842. https://doi.org/10.1021/acs.langmuir.3c02332.
37. Vishvakarma VK, Shukla N, Kumari K, Patel R, Singh P (2019) A model to study the inhibition of nsP2B-nsP3 protease of dengue virus with imidazole, oxazole, triazole thiadiazole, and thiazolidine based scaffolds. Heliyon 5:e02124. https://doi.org/10.1016/j.heliyon.2019.e02124.
38. Kumar A, Kumar D, Kumari K, Mkhize Z, Seru LK, Bahadur I, Singh P (2021) Metal-ligand complex formation between ferrous or ferric ion with syringic acid and their anti-oxidant and anti-microbial activities: DFT and molecular docking approach. J Mol Liq 322:114872. https://doi.org/10.1016/j.molliq.2020.114872.
39. Lu T, Chen F (2012) Multiwfn: A multifunctional wavefunction analyzer. J Comput Chem 33:580-592. https://doi.org/10.1002/jcc.22885.
40. Li Y, Javed R, Li R, Zhang YY, Lang ZY, Zhao HB, Liu X, Cao HM, Ye DX (2023) A colorimetric smartphone-based sensor for on-site AA detection in tropical fruits using Fe-P/NC single-atom nanoenzyme. Food Chem 406:135017. https://doi.org/10.1016/j.foodchem.2022.135017.
41. Quan ZL, Luo CY, Zhu BT, Zhao CG, Yang MY, Bjørås M, Zhu KZ, Kjøniksen AL (2021) Synthesis and antimicrobial activities of chitosan/polypropylene carbonate-based nanoparticles. RSC Adv 11:10121-10129. https://doi.org/10.1039/D0RA09257F.

Figures

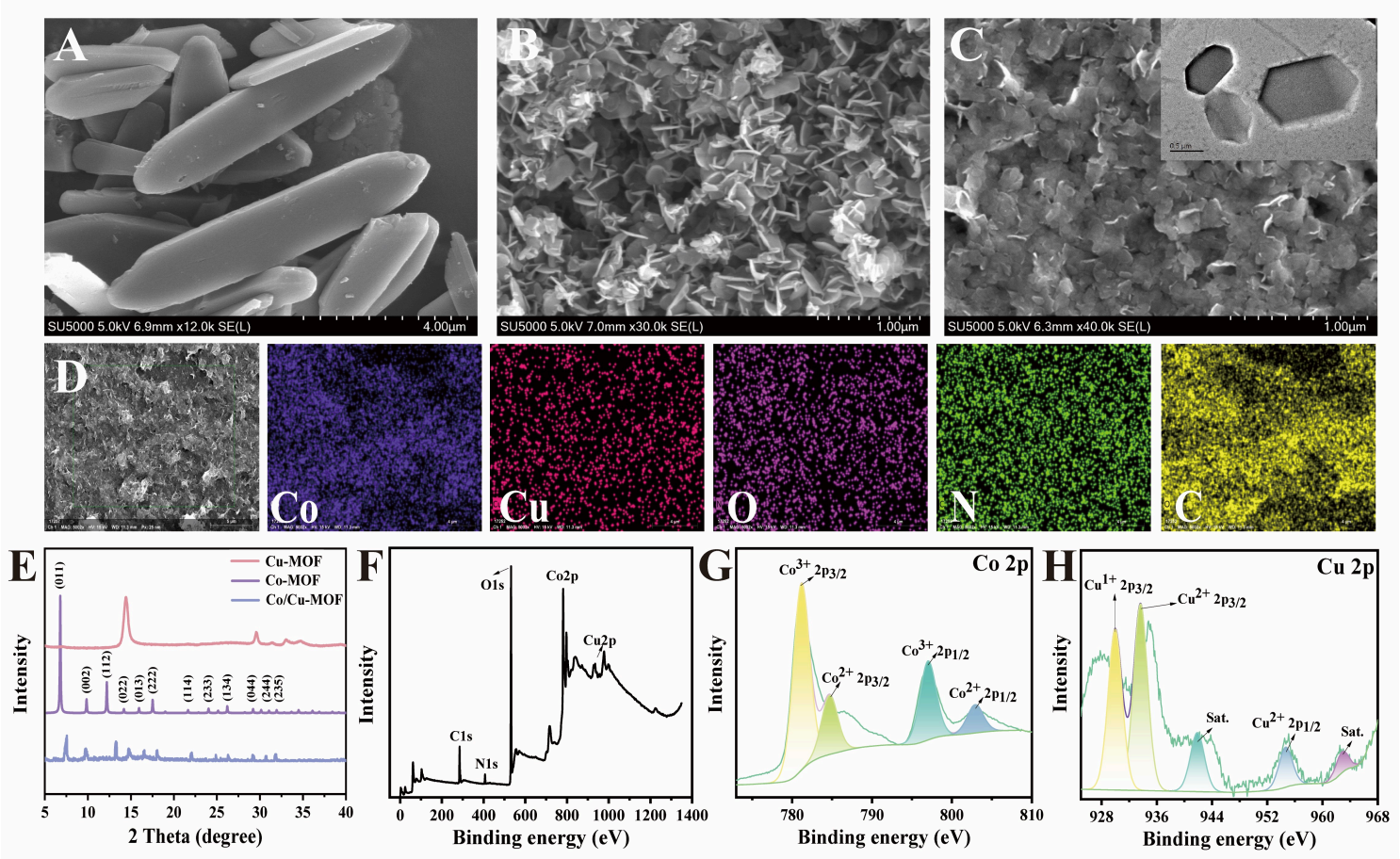


Figure 1

SEM images of (A) Co-MOF, (B) Cu-MOF and (C) Co/Cu-MOF(inset: TEM image of Co/Cu-MOF). (D) Elemental mapping of Co/Cu-MOF. (E) XRD profiles of Co-MOF, Cu-MOF and Co/Cu-MOF. (F) Full XPS spectra of Co/Cu-MOF. The high-resolution binding energy spectra of (G) Co 2p, and (H) Cu 2p.

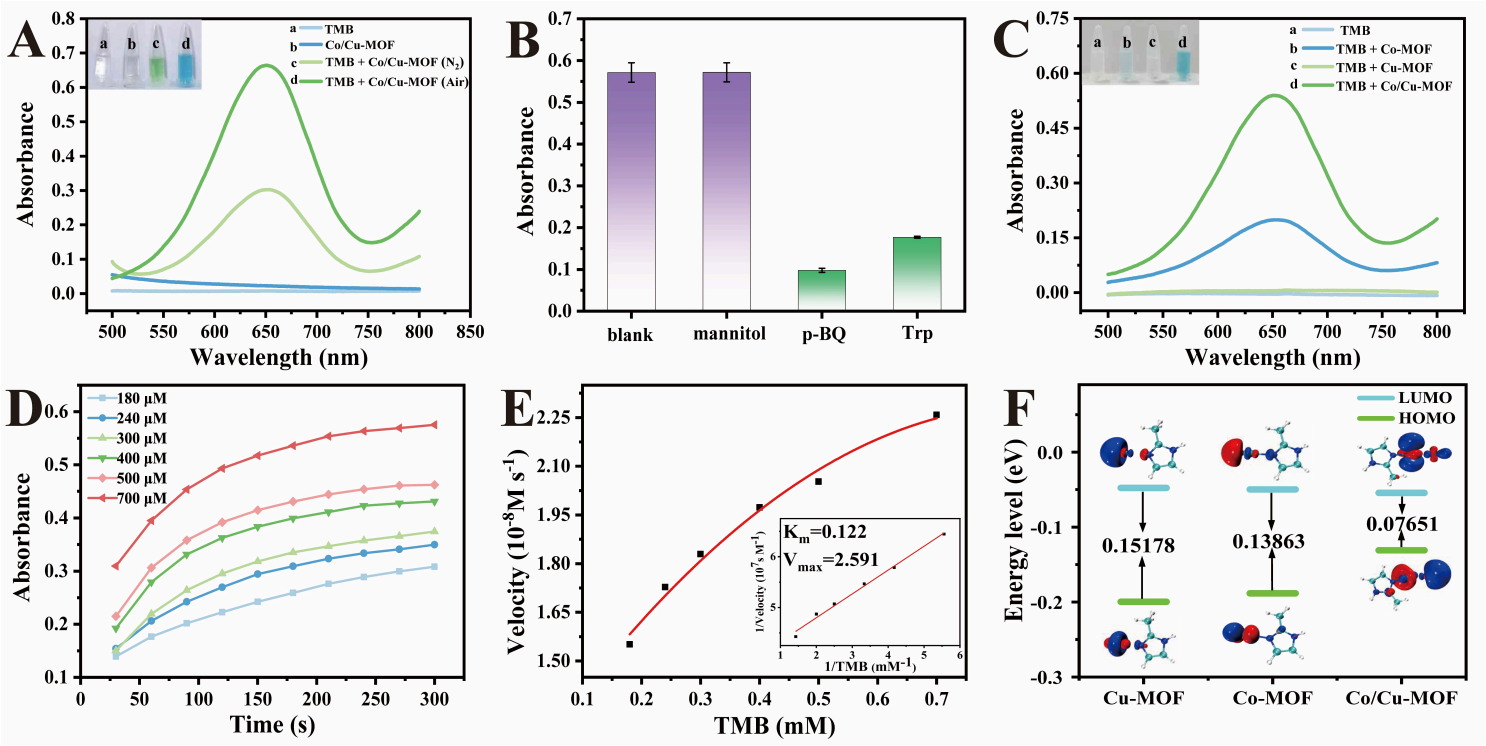


Figure 2

(A) UV-vis absorption spectra of Co/Cu-MOF-TMB system in air or N_2. Inset shows the corresponding color changes. (B) Analysis of ROS during Co/Cu-MOF catalysis. (C) UV-vis absorption spectra of different reaction systems. Inset shows the corresponding color changes. (D) Changes in the UV-vis absorbance values of the Co/Cu-MOF-TMB system at 652 nm with time and TMB concentration. (E) The Michaelis-Menten curve of Co/Cu-MOF at different TMB concentrations (inset: corresponding double reciprocal plots). (F) HOMO-LUMO energy level of the different materials.

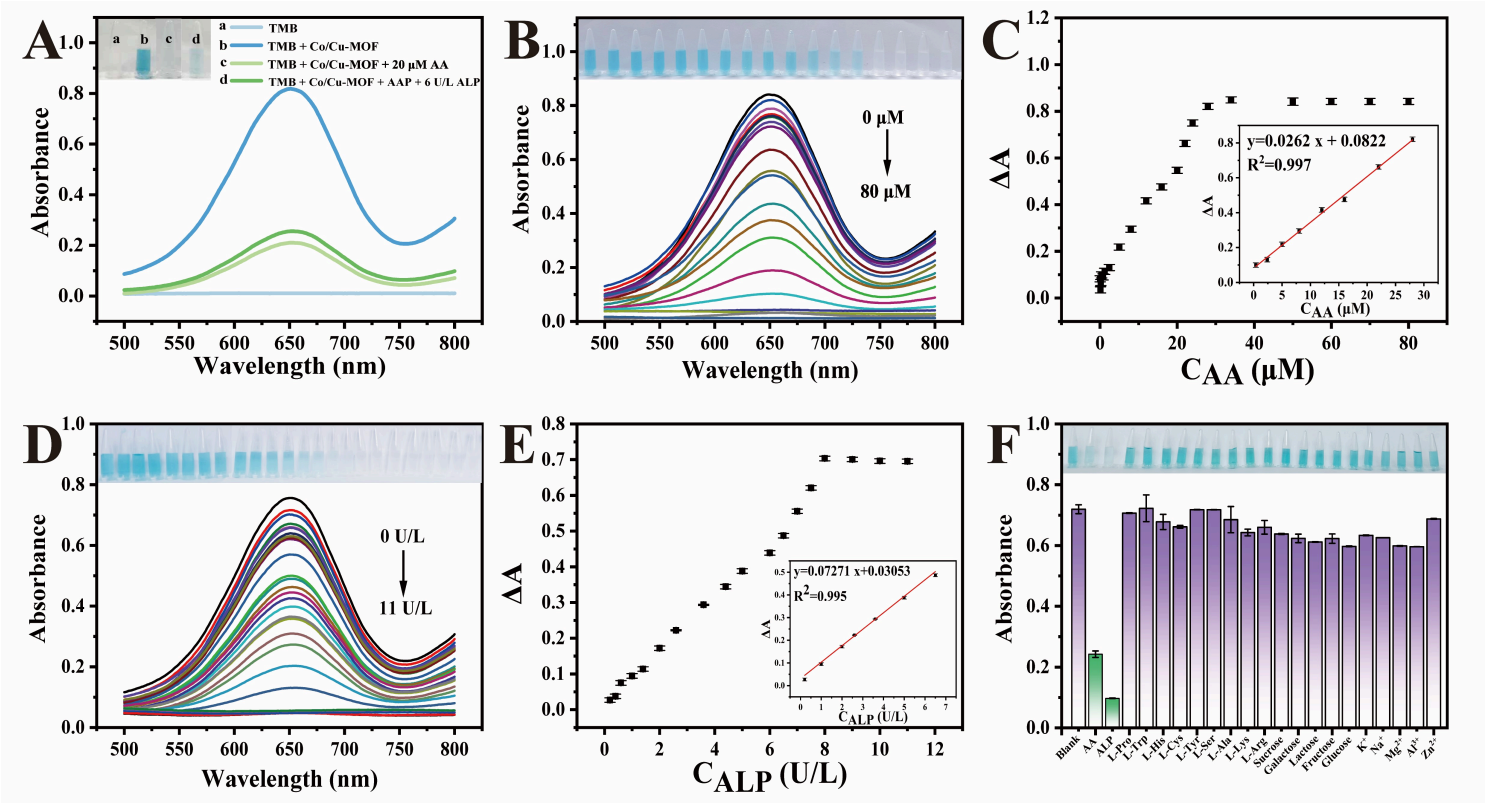


Figure 3

(A) Feasibility study for the detection of AA and ALP using the Co/Cu-MOF-TMB system (Inset shows the corresponding photographs). UV-vis absorbance spectra of the Co/Cu-MOF-TMB system with different concentrations of (B) AA and (D) ALP; Inset shows the corresponding photographs. Calibration curves of (C) AA and (E) ALP detection; the insets present the linear calibration curves. (F) Selectivity test for AA and ALP in the presence of potential interferents; Inset shows the corresponding photographs. Conditions: 20 μM AA; 6 U/L ALP; 200 μM other interferents.

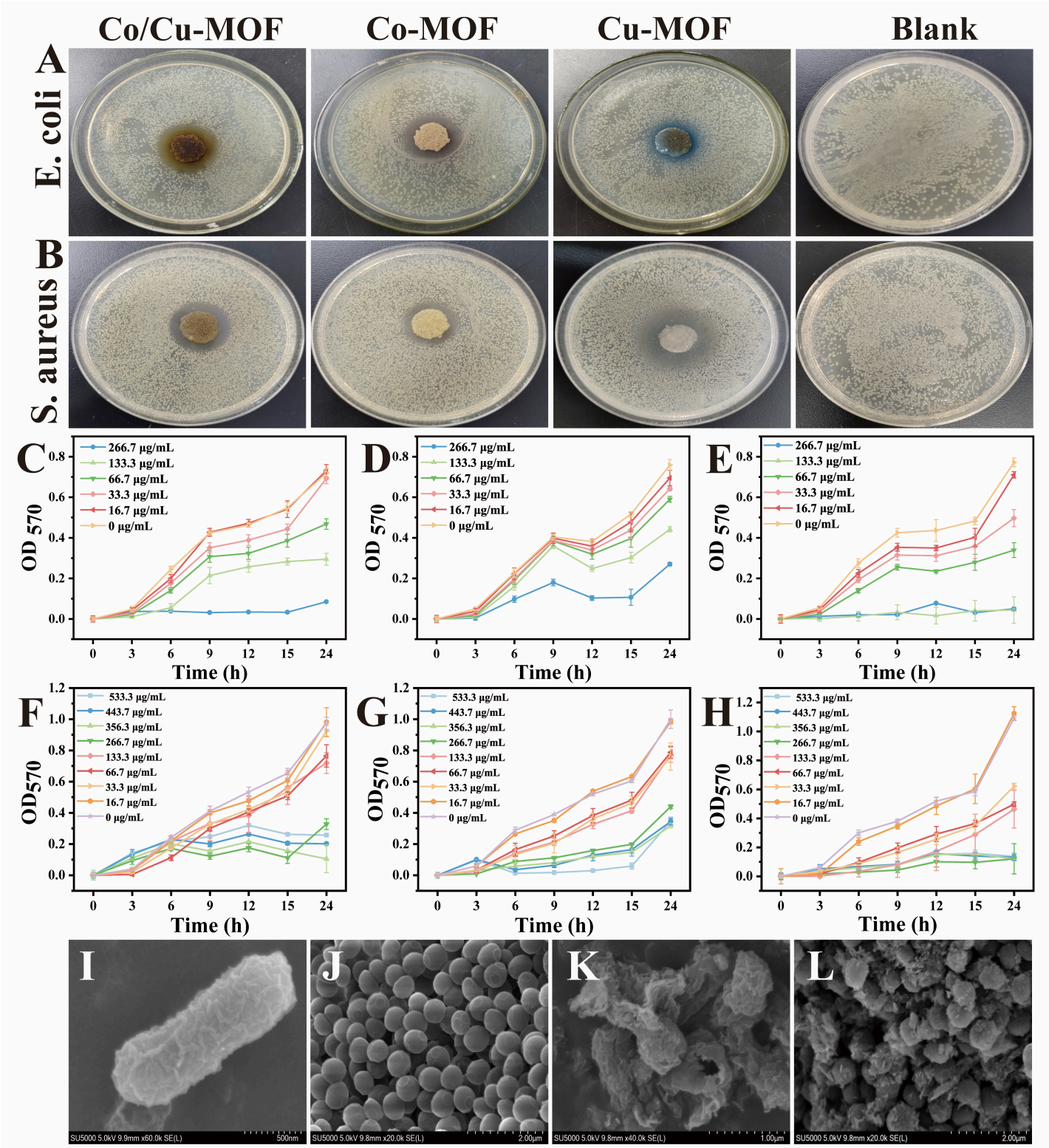


Figure 4

Photographs of the zones of inhibition for the different materials against *E. coli* (A) and *S. aureus* (B). Growth curves of *E. coli* after treatment with different concentrations of (C) Co-MOF, (D) Cu-MOF and (E) Co/Cu-MOF respectively. Growth curves of *S. aureus* after treatment with different concentrations of (F) Co-MOF, (G) Cu-MOF and (H) Co/Cu-MOF, respectively. SEM morphological images of *E. coli* (I, K) and *S. aureus* (J, L) before and after treatment with the Co/Cu-MOF.

Supplementary Files

This is a list of supplementary files associated with this preprint. Click to download.

- supportinginformation.docx
- Supplementalfiles.docx
- tables.docx
- GraphicalAbstract.docx